ChemSusChem

Research Article
doi.org/10.1002/cssc.202500802

Chemistry Europe
European Chemical Societies Publishing

www.chemsuschem.org

Ruthenium/Carbon Nanocomposites for Efficient Hydrogen Electrocatalysis: Impacts of Halide Residues

Bingzhe Yu, Qiming Liu, Chaochao Dun, Davida Briana DuBois, Bryan Hou, Dingjie Pan, John Tressel, Kiley Mayford, Colton Jones, Xiao Wang, Qingfeng Ge, Frank Bridges, and Shaowei Chen*

Ruthenium has emerged as a promising substitute for platinum toward the hydrogen evolution/oxidation reaction (HER/HOR). Herein, ruthenium/carbon composites are prepared by magnetic induction heating (300 A, 10 s) of $RuCl_3$, $RuBr_3$ or RuI_3 loaded on hollow N-doped carbon cages (HNC). The HNC-$RuCl_3$-300A sample consists of Ru nanoparticles (dia. 1.96 nm) and abundant Cl residues. HNC-$RuBr_3$-300A possesses a larger nanoparticle size (≈19.36 nm) and lower content of Br residues. HNC-RuI_3-300A contains only bulk-like Ru agglomerates with a minimal amount of I residues, due to reduced Ru-halide bonding interactions. Among these, HNC-$RuCl_3$-300A exhibits the best HER activity in alkaline media, with a low overpotential of only −26 mV to reach 10 mA cm^{-2}, even outperforming Pt/C, and can be used as the cathode catalyst for anion exchange membrane water electrolyzer (along with commercial RuO_2 as the anode catalyst), producing 0.5 A cm^{-2} at 1.88 V for up to 100 h, a performance markedly better than that with Pt/C. HNC-$RuCl_3$-300A also exhibits the best HOR activity, with a half-wave potential (+18 mV) even lower than that of Pt/C (+35 mV). These activities are ascribed to the combined contributions of small Ru nanoparticles and Ru-to-halide charge transfer that weaken H adsorption.

1. Introduction

To mitigate the pressing issue of the depletion of fossil fuels, researchers are turning to renewable and sustainable energy sources, among which hydrogen has been hailed as the "fuel of the future".[1,2] In fact, hydrogen fuel cells have been attracting extensive attention as a sustainable energy technology, featuring high efficiency and zero emissions, and have found diverse applications in transportation, stationary power generation, and portable electronics, among others.[3,4] Yet, the widespread application of hydrogen fuel cells is hampered by a range of challenges, in particular, energy-intensive production and costly storage and transportation of the hydrogen gas.[5] One viable solution is to produce hydrogen via water electrolysis driven by renewable energy such as solar and wind power.[6,7]

There are two key half reactions in these energy technologies, the hydrogen evolution reaction (HER) in water splitting and the hydrogen oxidation reaction (HOR) in hydrogen fuel cells, both of which require appropriate catalysts to boost the electron-transfer kinetics such that a high current density can be produced to meet practical demands.[8,9] Pt-based nanoparticles have been the catalysts of choice for both HER and HOR; yet, the high cost and low earth abundance of platinum hinder the development.[10,11] Ruthenium has emerged as a promising alternative, thanks largely to a relatively low cost (≈40% of Pt) and similar hydrogen binding energy (≈65 kcal mol^{-1}) to that of Pt.[12–15] Mechanistically, Ru is located on the left side of the volcano plot of hydrogen adsorption free energy (ΔG_{H^*}), suggestive of a somewhat too strong H adsorption that is nonideal for the desorption of H_2 after reaction on the catalyst surface.[16–18] This also means that the HER and HOR performance can be enhanced by slightly weakening H adsorption. To date, a range of strategies have been explored towards this goal. For instance, Wu et al.[19] prepared Cu—Ru alloy by ammonium sulfate etching to remove metallic Mn from Ru—Cu—Mn ribbons obtained via arc melting, and the $Cu_{53}Ru_{47}$ sample exhibited the highest HER activity with a low overpotential (η_{10}) of −15 mV to reach the current density of 10 mA cm^{-2}. This was ascribed to Cu alloying that weakened the Ru—H interaction, as Cu resides on the right side of the HER volcano plot. The alloying strategy has also been applied to HOR electrocatalysis. Yang et al.[20] synthesized Pt@Ru alloy nanoparticles (<3 nm) by sequential reduction of Pt and Ru at varied annealing temperatures and observed a low HOR half-wave potential ($E_{1/2}$) of +12.3 mV in alkaline media, with a

B. Yu, Q. Liu, D. B. DuBois, B. Hou, D. Pan, J. Tressel, C. Jones, X. Wang, F. Bridges, S. Chen
Department of Chemistry and Biochemistry
University of California
1156 High Street, Santa Cruz, CA 95064, USA
E-mail: shaowei@ucsc.edu

C. Dun
The Molecular Foundry
Lawrence Berkeley National Laboratory
Berkeley, CA 94720, USA

K. Mayford, F. Bridges
Department of Physics
University of California
1156 High Street, Santa Cruz, CA 95064, USA

Q. Ge
School of Chemical and Biomolecular Sciences
Southern Illinois University
Carbondale, IL 62901, USA

Supporting information for this article is available on the WWW under https://doi.org/10.1002/cssc.202500802

mass-normalized exchange current density ($j_{0,m}$) 8.0 times that of commercial Pt/C and the corresponding area-normalized exchange current density ($j_{0,ECSA}$) 5.8 times greater. In another study, Su et al.[21] deposited Ru nanoparticles on Co single atoms embedded within O-doped graphene (OG) and observed a remarkably enhanced HER activity in alkaline media ($\eta_{10} = -13$ mV), as compared to that without Co single atoms ($\eta_{10} = -48$ mV), due to charge transfer from the Ru cluster to the Co_1/OG scaffold.

Engineering of the coordination environment and electronic structure represents another strategy for catalyst design. For instance, Li et al.[22] prepared Ru nanoclusters anchored on N, S-codoped carbon nanosheets (Ru—S/N–C), which featured an η_{10} (-10 mV) markedly lower than that (-29 mV) of the S-free counterpart, because the incorporation of S dopants led to charge redistribution and weakened the H adsorption on Ru. In a more recent study, Wang et al.[23] synthesized amine-modulated Ru nanoclusters and observed an electrocatalytic activity towards both HOR ($E_{1/2} = +25$ mV) and HER ($\eta_{10} = -13$ mV) in alkaline media due to a downshift of the d-band center of Ru caused by the amine ligands. Notably, according to the d-band theory,[24,25] the lower the d-band center (in energy) relative to the Fermi level, the weaker the binding strength between the transition metals and adsorbates. Crystal phase modulation has also been exploited as a practical strategy to manipulate H adsorption. Zheng et al.[26] prepared anomalous face-centered cubic (fcc) Ru nanoparticles on a graphitic carbon nitride/carbon ($g\text{-}C_3N_4$/C) substrate and observed an enhanced HER activity ($\eta_{10} = -79$ mV) as compared to that of hexagonal close-packed (hcp) Ru/C ($\eta_{10} = -120$ mV), which was ascribed to favorable H adsorption on fcc Ru(100) as compared to that on hcp Ru(0001). Similarly, He et al.[27] synthesized fcc Ru nanocrystals using an ammonia-induced method and observed a superior performance in both HOR and HER as compared to hcp Ru/C, due to a negative shift of the Ru d-band center and weakened H adsorption on Ru.

Surface modification by heteroanion residues has recently been found to also impact the electrocatalytic activity. Such a unique feature is generally observed in samples prepared by ultrafast synthesis, due to incomplete decomposition of the metal salt precursors. For instance, Zhang et al.[28] prepared axial ligand-modified Pt single atom catalysts on NiFe-layered double hydroxide nanoarrays by an irradiation-impregnation strategy. Among the sample series, the chlorine-modified sample (Cl-Pt/LDH) was found to exhibit the best HER activity ($\eta_{10} = -25.2$ mV) in 1 M KOH, due to the strong electronic interaction between Cl and Pt single atoms that induced Pt-to-Cl charge transfer and hence weakened H adsorption on Pt. In another study, Wu et al.[29] prepared halogen-decorated Ru/RuP_2 heterojunction composites via a microwave procedure, and the bromine-modified sample (Br-Ru/RuP_2) stood out among the series of samples with a low η_{10} of -34 mV, due to a favorable ΔG_{H^*}. In a more recent study,[30] we prepared carbon-supported ruthenium nanoparticles by magnetic induction heating (MIH) of $RuCl_3$ on carbon paper. As the samples were prepared within seconds, the Ru nanoparticles featured a Cl-enriched surface that was unattainable via conventional pyrolysis, and the samples decorated with $RuCl_x$ residues exhibited the best HER activity in both acidic and alkaline media with a low η_{10} of -23 and -12 mV, respectively, highly comparable to that of commercial Pt/C. The superior HER activity was ascribed to the surface metal-Cl species that facilitated charge transfer and downshifted the d-band center of Ru. One immediate question arises. How will other halogen residues impact the electrocatalytic activity, given the marked difference in their electronegativity and hence electronic interactions with the metal centers? This is the primary motivation of the present work.

Herein, we prepared Ru nanoparticles decorated with various halide residues by MIH treatment at 300 A for 10 s of ruthenium(III) halides (i.e., $RuCl_3$, $RuBr_3$, and RuI_3) loaded on hollow N-doped carbon cages (HNC) pyrolytically derived from chemically etched zeolitic imidazolate framework-8 (ZIF-8). The Ru nanoparticles were found to increase in size, and concurrently, the content of halide residues diminished from $RuCl_3$ to RuI_3. Among the series, the sample derived from $RuCl_3$ (HNC-$RuCl_x$-300A) exhibited the best HER activity in 1 M KOH, with an η_{10} of -26 mV and Tafel slope of 26.5 mV dec^{-1}, outperforming commercial Pt/C. When the sample was used as the cathode catalyst for an anion exchange membrane water electrolyzer (AEMWE), the cell achieved a current density of 0.5 A cm^{-2} at a low voltage of 1.88 V and exhibited stable operation for 100 h. HNC-$RuCl_3$-300A also exhibited the best HOR activity among the series, delivering an anodic current density comparable to that of Pt/C, with a low $E_{1/2}$ of $+18$ mV compared to $+35$ mV for Pt/C. Results from density functional theory (DFT) calculations showed that the enhanced electrocatalytic activity of HNC-$RuCl_3$-300A could be attributed to the combined contributions of the small size of the Ru nanoparticles and the surface Cl residues that weakened H adsorption by charge transfer from the Ru nanoparticles, in comparison to the Br and I modified counterparts.

2. Results and Discussion

2.1. Sample Synthesis and Structural Characterization

The preparation of the HNC-RuX_3 nanocomposites was schematically illustrated in **Figure 1**a, which consisted of four major steps. First, hollow ZIF-8 was prepared by tannic acid etching of ZIF-8.[31] Second, HNC was obtained via pyrolysis of the hollow ZIF-8 at 900 °C for 3 h in a nitrogen atmosphere. Third, a controlled amount of ruthenium(III) halide (RuX_3, X = Cl, Br, or I) was evenly distributed onto HNC by freeze-drying. Fourth, the precursors were treated by MIH at different induction currents for 10 s. During MIH, the Joule's effect led to a quick temperature rise (over 1000 °C) within a few seconds (Figure S1, Supporting Information).[30,32,33]

The sample structures were first examined using transmission electron microscopy (TEM) measurements. From Figure 1b–d, one can see that the hollow dodecahedral morphology of the etched ZIF-8 precursor was largely retained for all samples after MIH treatment, with a size of ≈400 nm. Against the carbon scaffold, dark-contrast nanoparticles can be found with the HNC-$RuCl_3$-300A (dia. 1.96 ± 0.55 nm, Figure 1e and S2a) and

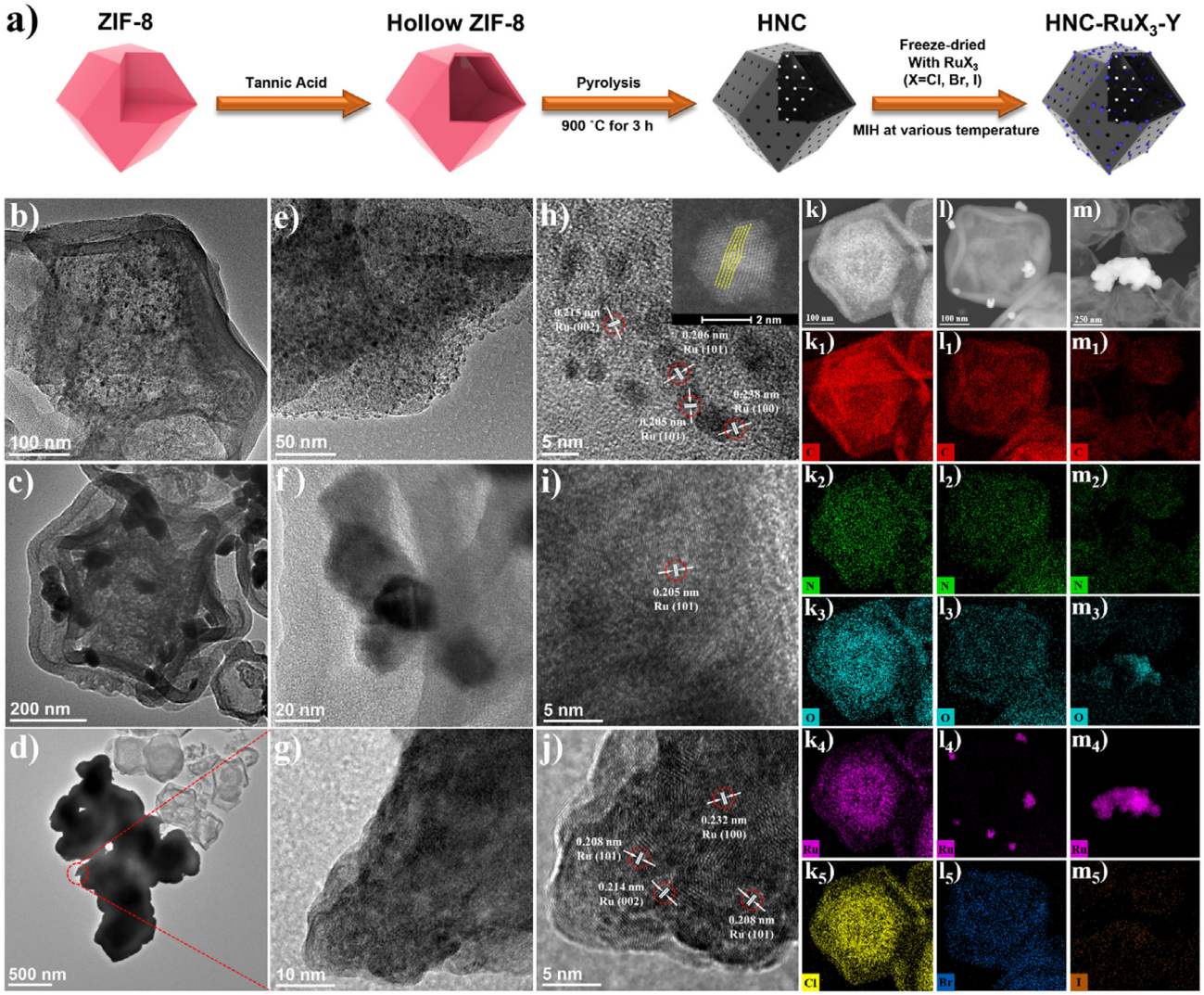

Figure 1. a) Schematic illustration of the rapid preparation of HNC-RuX_3-Y composites by MIH, TEM images of b,e,h) HNC-$RuCl_3$-300A (inset to panel h is a HAADF-STEM image), c,f,i) HNC-$RuBr_3$-300A, and d,g,j) HNC-RuI_3-300A. TEM images of k) HNC-$RuCl_3$-300A, l) HNC-$RuBr_3$-300A, and m) HNC-RuI_3-300A, with the corresponding EDS-based elemental maps shown in k_1–k_5), l_1–l_5), and m_1–m_5), respectively (C red, N green, O cyan, Ru purple, Cl yellow, blue Br, and orange I). Scale bars are (b,c) 100 nm, (d) 500 nm, (e,f) 50 nm, (g) 10 nm, (h,i,j) 5 nm, (k) 100 nm, (l) 100 nm, and (m) 250 nm.

HNC-$RuBr_3$-300A (dia. 19.36 ± 3.03 nm, Figure 1f and S2b) samples, whereas only chunky agglomerates with HNC-RuI_3-300A (a few hundred nm in size, Figure 1d,g). In high-resolution TEM measurements, the nanoparticles can be seen to exhibit clearly-defined lattice fringes (Figure 1h–j), with interplanar distances of 0.205, 0.215, and 0.238 nm that can be ascribed to the (101), (002), and (100) planes of hcp Ru (PDF 06-0663), respectively.[34–36] This suggests successful formation of carbon-supported ruthenium nanoparticles. Consistent results were obtained in high-angle annular dark-field scanning transmission electron microscopy (HAADF-STEM) measurements, where HNC-$RuCl_3$-300A can be seen to possess markedly smaller nanoparticles (and clear edge dislocations) (Figure 1h inset and Figure S3, Supporting Information) than HNC-$RuBr_3$-300A (Figure S4, Supporting Information).

In elemental mapping analysis based on energy-dispersive spectroscopy (EDS) (Figure 1k–m), one can see that the C, N, and O elements were distributed rather evenly across the series of samples, suggesting effective graphitization of the ZIF-8 precursor by MIH treatment. For HNC-$RuCl_3$-300A, the Ru and Cl elements can be found to exhibit an apparent overlap and were enriched within the nanoparticles, indicative of surface functionalization of the nanoparticles by the Cl residues[30] (Figure 1k_1–k_5 and Figure S2c, Supporting Information). By contrast, Br and I were distributed rather evenly throughout HNC-$RuBr_3$-300A (Figure 1l_1–l_5 and S2d, Supporting Information) and HNC-RuI_3-300A (Figure 1m_1–m_5 and S2e, Supporting Information), whereas the Ru signals were mostly confined within the nanoparticles and agglomerates.

The discrepancy of the sample morphologies and elemental distributions observed above may be accounted for by the different bond dissociation energy, which decreases in the order of Ru—Cl > Ru—Br > Ru—I, consistent with the halogen electronegativity and atomic size.[37] Thus, during MIH treatment, the ready thermal decomposition of RuI_3 led to the formation of large agglomerates in HNC-RuI_3-300A; yet for $RuBr_3$, the thermal decomposition was impeded somewhat, producing only

nanoparticles in HNC-$RuBr_3$-300A, and the nanoparticles became even smaller in HNC-$RuCl_3$-300A due to the strongest Ru—Cl interactions.

Indeed, from the in situ X-ray diffraction (XRD) patterns acquired with RuX_3 at different temperatures (**Figure 2**a–c), one can see that the characteristic peaks of metallic Ru ($2\theta = 38.4°$, 42.2°, and 44.0°) started to become visible at ≈400 °C for $RuCl_3$, and at a somewhat lower temperature of ≈300 °C for $RuBr_3$ and RuI_3. Furthermore, while the peaks became intensified with increasing temperatures for all samples, they were markedly broader for $RuCl_3$ than for the other two, in good agreement with the smaller size of the Ru nanoparticles observed above with HNC-$RuCl_3$-300A as compared to HNC-$RuBr_3$-300A and HNC-RuI_3-300A.

Figure 2d displays the N_2 adsorption-desorption isotherms of HNC, HNC-$RuCl_3$-300A, HNC-$RuBr_3$-300A, and HNC-RuI_3-300A. One can see that all samples exhibited a Type IV isotherm with a hysteresis loop characteristic of mesopores.[38] The specific surface area based on the Brunauer–Emmett–Teller (BET) model was estimated to be 162.3 $m^2 g^{-1}$ for HNC, and diminished somewhat to 157.63 $m^2 g^{-1}$ for HNC-$RuCl_3$-300A, 153.51 $m^2 g^{-1}$ for HNC-$RuBr_3$-300A, and 160.33 $m^2 g^{-1}$ for HNC-RuI_3-300A. The corresponding pore size distribution (diameter) profiles are shown in Figure 2e. The HNC sample can be seen to consist of two main peaks, a sharp peak at ≈1.8 nm corresponding to micropores and a broad peak at 7.3 nm to mesopores.[39] For the Ru-containing samples, the mesopore peak was suppressed markedly with the intensity varying in the order

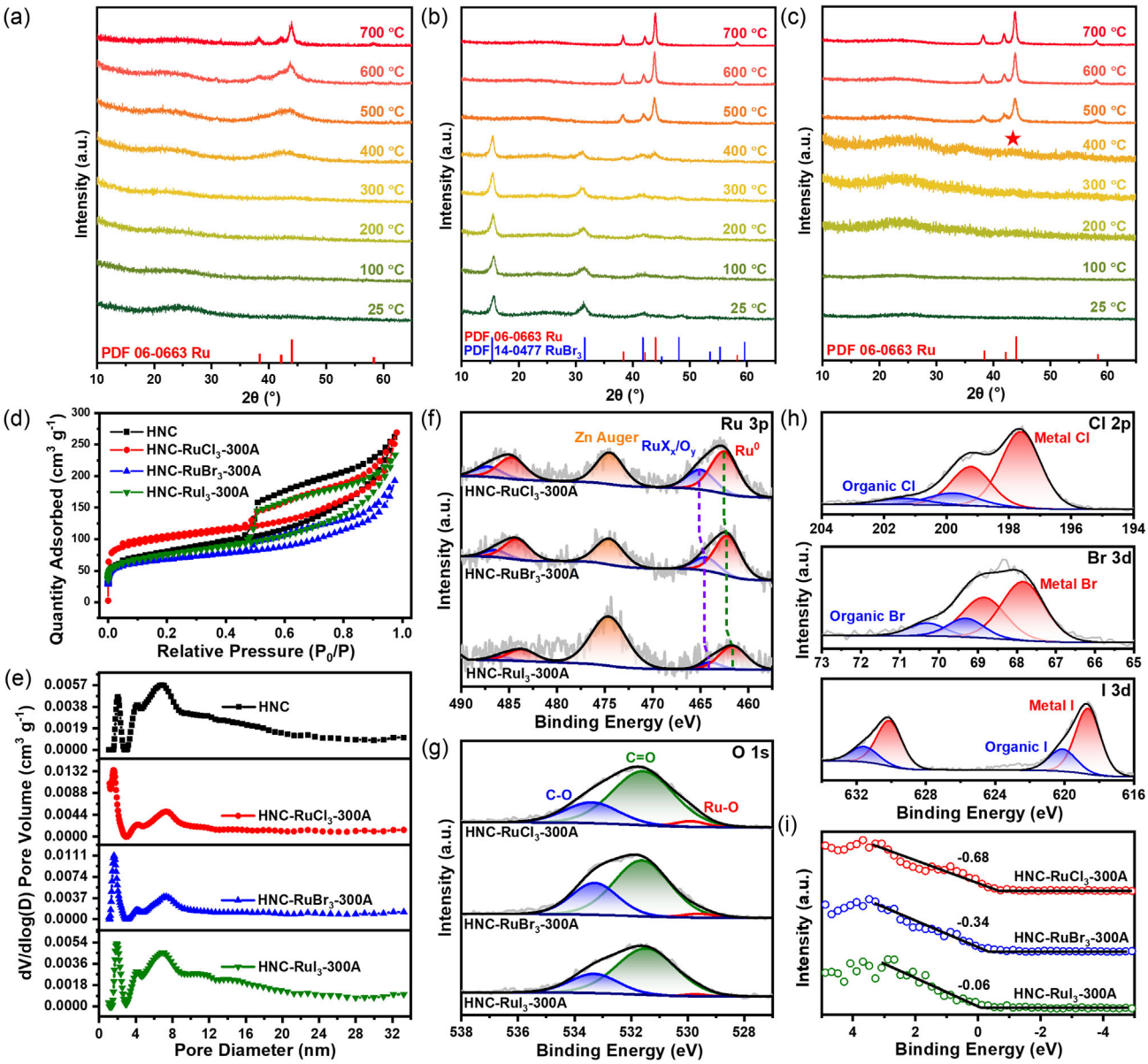

Figure 2. In situ XRD patterns of a) $RuCl_3$, b) $RuBr_3$, and c) RuI_3 acquired at different temperatures. d) Nitrogen adsorption–desorption isotherms of HNC, HNC-$RuCl_3$-300A, HNC-$RuBr_3$-300A, and HNC-RuI_3-300A, and e) the corresponding pore size distribution curves. High-resolution XPS spectra of the f) Ru 3*p*, g) O 1*s*, and h) Cl 2*p*, Br 3*d*, I 3*d* electrons of HNC-$RuCl_3$-300A, HNC-$RuBr_3$-300A, and HNC-RuI_3-300A. i) The corresponding VBM profiles.

of HNC-$RuCl_3$-300A < HNC-$RuBr_3$-300A < HNC-RuI_3-300A < HNC. This is in line with the formation of ruthenium nanoparticles that most likely occupied the mesopores, and such impacts diminished with the increasing agglomeration of Ru.[40]

The elemental composition and valency of the sample series were then examined using X-ray photoelectron spectroscopy (XPS) measurements. From the survey spectra in Figure S5a (Supporting Information), the C 1*s*, N 1*s*, Ru 3*p*, and O 1*s* electrons can be clearly identified for all samples at ≈286, 400, 464, 475, and 532 eV, respectively; for the HNC-$RuCl_3$ composites, additional peaks can be found at ≈198 eV for the Cl 2*p* electrons and 269 eV Cl 2*s*, and the Br 3*p* and 3*d* peaks at 182 and 69 eV for HNC-$RuBr_3$-300A, whereas the I 4*d* and 3*d* electrons at 49 and 619 eV for HNC-RuI_3-300A, respectively. Based on the integrated peak areas, the elemental contents were calculated and listed in Table S1 (Supporting Information). The Ru content can be seen to decrease from 0.45 at% for HNC-$RuCl_3$-300A to 0.25% for HNC-$RuBr_3$-300A and 0.11 at% for HNC-RuI_3-300A, along with 2.39 at% of Cl for HNC-$RuCl_3$-300A, 0.68 at% of Br for HNC-$RuBr_3$-300A, and 0.46 at% of I for HNC-RuI_3-300A, consistent with the increasing thermal volatility of the precursors from $RuCl_3$ to RuI_3.

Figure 2f shows the corresponding high-resolution scans of the Ru 3*p* electrons, which can be deconvoluted into two doublets. For HNC-$RuCl_3$-300A, the major doublet at ≈462.51/484.71 eV can be attributed to the $3p_{3/2}/3p_{1/2}$ electrons of metallic Ru, while the minor one at ≈464.99/487.19 eV to those of $Ru^{\delta+}$ species[41,42] (the peak at ≈474.5 eV likely due to Zn Auger of residual Zn from ZIF-8). Notably, these binding energies displayed a marked redshift for HNC-$RuBr_3$-300A (461.95/484.15 and 464.44/486.44 eV) and HNC-RuI_3-300A (461.64/483.64 and 463.99/483.99 eV) (Table S2, Supporting Information), suggesting electron enrichment from HNC-$RuCl_3$-300A to HNC-RuI_3-300A because of the different thermal stability of the RuX_3 precursors. In fact, the Ru^0: $Ru^{\delta+}$ atomic ratio can be seen to increase in the order of HNC-$RuCl_3$-300A (2:1) < HNC-$RuBr_3$-300A (3:1) < HNC-RuI_3-300A (4.5:1) (Table S3, Supporting Information), consistent with the increasing nanoparticle size observed in the above TEM measurements.

The corresponding O 1*s* spectra are shown in Figure 2g, where all samples can be seen to possess two major peaks, C═O at 531.63 eV and C—O at 533.43 eV, with a very minor one at 529.92 eV for metal-O.[43] Figure 2h depicts the Cl 2*p* spectrum of HNC-$RuCl_3$-300A, Br 3*d* of HNC-$RuBr_3$-300A, and I 3*d* of HNC-RuI_3-300A. HNC-$RuCl_3$-300A can be seen to consist of a major doublet at ≈197.62/199.22 eV due to metal-Cl species and a minor one at 199.81/201.41 eV due to organic Cl.[44,45] Similarly, HNC-$RuBr_3$-300A and HNC-RuI_3-300A also possessed two doublets, the metal-Br species at 67.86/68.86 eV and the organic Br at 69.33/70.33 eV for the former,[46,47] whereas the metal-I at 618.67/630.17 eV and organic I at 620.15/631.65 eV.[48] Notably, the contents of the metal-halide residues decreased markedly from HNC-$RuCl_3$-300A (1.98 at% Ru-Cl) to HNC-$RuBr_3$-300A (0.54 at% Ru-Br) and further to HNC-RuI_3-300A (0.34 at% Ru-I) (Table S3, Supporting Information). These observations are in alignment with results from the EDS-based elemental mapping analysis (Figure 1k–m).

The C 1*s* spectra for the series of samples are shown in Figure S6a (Supporting Information), where the C—C/C═C (284.6 eV), C—O (286.1 eV), C═O (288.4 eV), and Ru 3*d* peaks (≈282 eV) can be clearly resolved. Additionally, pyridinic N (398.3 eV), pyrrolic N (400.0 eV), and graphitic N (401.3 eV) can be deconvoluted in the N 1*s* spectra (Figure S6b, Supporting Information). This confirms the successful transformation of the ZIF-8 precursor to N-doped carbon.

Figure 2i shows the corresponding valence band maximum (VBM) profiles. All samples can be seen to possess a negative VBM, which upshifted from HNC-$RuCl_3$-300A (−0.68 eV) to HNC-$RuBr_3$-300A (−0.34 eV) and further to HNC-RuI_3-300A (−0.06 eV). This is in good agreement with the structural transition from nanosized particles in HNC-$RuCl_3$-300A to bulk metallike in HNC-RuI_3-300A.[49,50]

Consistent results were obtained from X-ray absorption spectroscopy (XAS) measurements. **Figure 3**a shows the Ru K-edge X-ray absorption near-edge structure (XANES) of the sample series. It can be clearly seen that the absorption edges were at a slightly higher energy than that of Ru foil but significantly lower than that of RuO_2, suggesting an average valence state close to that of metallic Ru. In fact, the absorption edge energy and white line intensity both increase in the order of Ru foil < HNC-RuI_3-300A < HNC-$RuBr_3$-300A < HNC-$RuCl_3$-300A < RuO_2, suggesting an increasing Ru valence state, in good agreement with results from XPS measurements (Figure 2f).

Figure 3b exhibits the corresponding Fourier transforms of the extended X-ray absorption fine structure (FT-EXAFS) spectra, which featured a major peak at ≈2.44 Å consistent with the Ru—Ru path in Ru foil, along with a minor one at ≈1.50 Å likely for Ru—O. Note that HNC-$RuCl_3$-300A also possessed a shoulder at ≈1.80 Å that can be assigned to Ru—Cl, and this shoulder became drastically weaker in HNC-$RuBr_3$-300A and almost invisible in HNC-RuI_3-300A, consistent with the diminishing Ru—X content as manifested in XPS measurements (Table S3, Supporting Information). From the fitting results in Figure S7 (Supporting Information) and Table S4 (Supporting Information), it can be seen that whereas the Ru—Ru bond length was rather consistent at ≈2.68 Å, the coordination number (CN) increased from ≈3.8 for HNC-$RuCl_3$-300A to 6.1 for HNC-$RuBr_3$-300A and 9.4 for HNC-RuI_3-300A, consistent with the growing size of the Ru particles, as observed in TEM measurements (Figure 1). Concurrently, the Ru—O bond length was very close at ≈1.98 Å for the samples, yet the CN diminished in the order of HNC-$RuCl_3$-300A (2.8) to HNC-$RuBr_3$-300A (1.5) < HNC-RuI_3-300A (0.4), indicative of a drastically decreasing oxide component in the samples, in agreement with results from the above XPS measurements (Figure 2g).

To further investigate the coordination environment, the corresponding wavelet transforms (WT) of the EXAFS data are shown in Figure 3c. One can see that all samples possessed a major peak at (8.96 $Å^{-1}$, 2.33 Å) due to the Ru—Ru path and a minor one at (4.42 $Å^{-1}$, 1.45 Å) for the Ru—O path. In fact, the intensity ratio of the Ru—O and Ru—Ru peaks decreased significantly from HNC-$RuCl_3$-300A to HNC-$RuBr_3$-300A and HNC-RuI_3-300A, consistent with the increasingly metallic characters in the samples (Figure 2g).

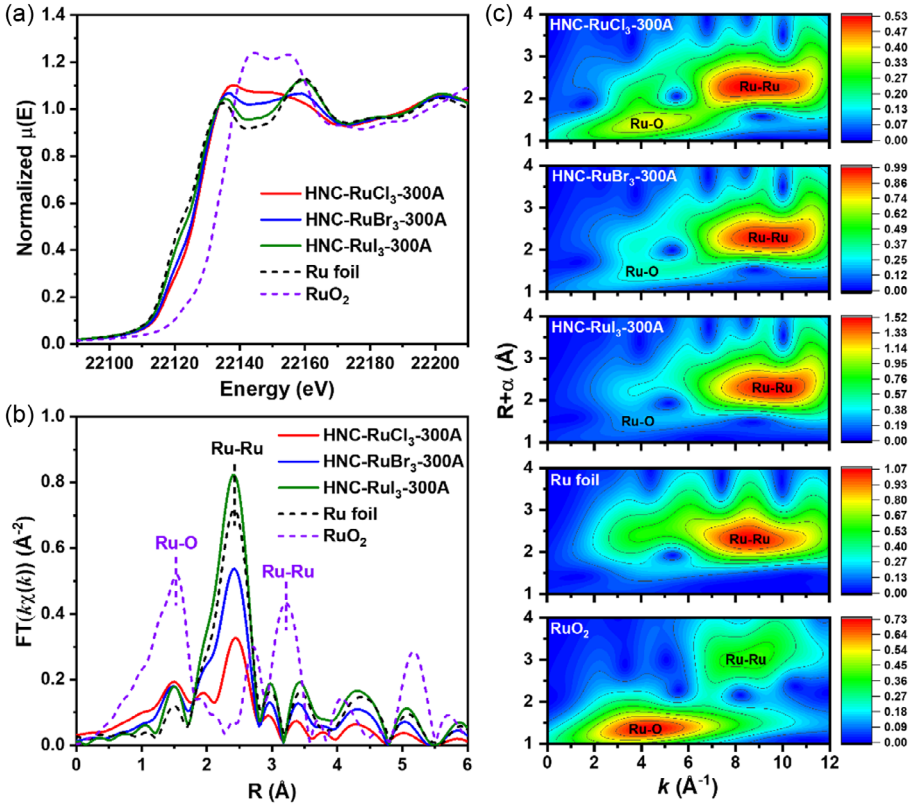

Figure 3. a) Ru K-edge XANES spectra, b) Fourier transforms of the EXAFS spectra, and c) WT-EXAFS maps of HNC-$RuCl_3$-300A, HNC-$RuBr_3$-300A, HNC-RuI_3-300A, Ru foil, and commercial RuO_2.

Taken together, results from these structural characterizations show that the HNC-RuX_3-300A composites prepared above all consisted of carbon-supported Ru nanoparticles decorated with halogen residues, but the nanoparticle size increased, and the amount of halogen residues diminished, from HNC-$RuCl_3$-300A to HNC-RuI_3-300A.

2.2. Electrocatalytic Activity

The HER activity of the sample series was then examined and compared. **Figure 4**a shows the HER polarization curves of the HNC-RuX_3-300A samples in 1 M KOH. One can see that HNC-$RuCl_3$-300A showed the highest catalytic activity among the series, with the lowest η_{10} of −26 mV, in comparison to −115 mV for HNC-$RuBr_3$-300A, −385 mV for HNC-RuI_3-300A, and over −600 mV for HNC. In fact, HNC-$RuCl_3$-300A even outperformed commercial- Pt/C (−40 mV). In terms of mass activity (HER currents normalized to Ru mass), HNC-$RuCl_3$-300A, again, stood out as the best catalyst (Figure S8, Supporting Information). At the overpotential of −50 mV, HNC-$RuCl_3$-300A exhibited a turnover frequency of 2.14 s^{-1}, significantly higher than those of HNC-$RuBr_3$-300A (0.31 s^{-1}), HNC-RuI_3-300A (0.03 s^{-1}), and even Pt/C (0.35 s^{-1}) (Figure S9, Supporting Information). The corresponding Tafel plots are shown in Figure 4b, where HNC-$RuCl_3$-300A displays the lowest slope of 26.5 mV dec^{-1}, in comparison to Pt/C (32.7 mV dec^{-1}), HNC-$RuBr_3$-300A (68.7 mV dec^{-1}), and HNC-RuI_3-300A (196.0 mV dec^{-1}). This indicates the most facile electron-transfer kinetics of HNC-$RuCl_3$-300A among the sample series.

Such a variation of the HER performance can be ascribed to the electron-deficient Ru in HNC-$RuCl_3$-300A that was facilitated by the high-electronegativity Cl residues and hence weakened H adsorption, in comparison to HNC-$RuBr_3$-300A to HNC-RuI_3-300A.[17] In fact, for the HNC-$RuCl_3$-TF700 composite that was prepared using conventional pyrolysis in a tube furnace at a similar temperature (700 °C), despite a comparable Ru content, the sample exhibited a markedly reduced content of the Cl residues (Table S1, Supporting Information), and hence a significantly lower HER activity than that of HNC-$RuCl_3$-300A (Figure S10–S11, Supporting Information). A similar behavior was observed in HNC-$RuBr_3$-TF700 and HNC-RuI_3-TF700 (Figure S11, Table S1, Supporting Information). This confirms the significant role of anionic residues in dictating the HER activity of the nanocomposites.

The electrochemically active surface area (ECSA) of the sample series was then determined by CO stripping (Figure 4c and S12a, Supporting Information). One can see that the ECSA increased from 71.2 $m^2 g^{-1}$ (HNC-RuI_3-300A) to 83.1 $m^2 g^{-1}$ (HNC-$RuBr_3$-300A), and finally to 96.8 $m^2 g^{-1}$ for HNC-$RuCl_3$-300A, in line with the morphological evolution of Ru on the carbon scaffold (Figure 1). Consistent behaviors were observed from the double-layer capacitance (C_{dl}, Figure S12b, Supporting Information), which increased from 9.6 F cm^{-2} for HNC-RuI_3-300A, to 15.8 F cm^{-2} for HNC-$RuBr_3$-300A, 30.3 F cm^{-2} for HNC-$RuCl_3$-300A.

From the Nyquist plots in Figure 4d, one can see that HNC-$RuCl_3$-300A possessed the lowest the charge-transfer resistance

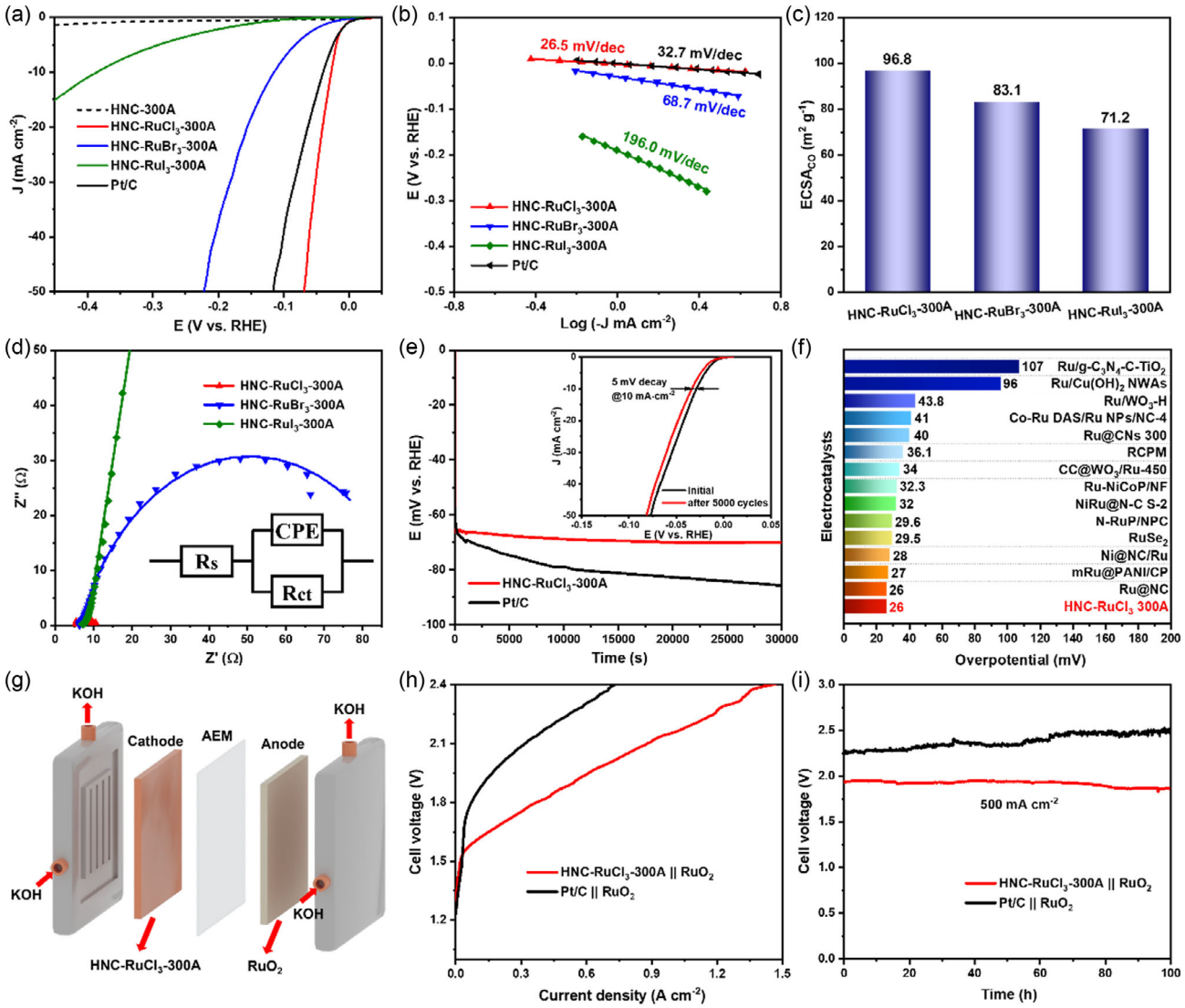

Figure 4. a) HER Polarization curves of the sample series in 1 M KOH, and b) the corresponding Tafel plots. c) Comparison of the ECSA measured by CO stripping. d) Nyquist plots at the potential of −100 mV. Inset is the equivalent circuit, where R_s is the uncompensated resistance, CPE is the constant-phase element, and R_{ct} is charge-transfer resistance. e) Chronopotentiometric curves of HNC-$RuCl_3$-300A and Pt/C at the current density of 10 mA cm^{-2}. The inset shows the polarization curves of HNC-$RuCl_3$-300A before and after 5000 CV cycles. f) Comparison of η_{10} between HNC-$RuCl_3$-300A and other state-of-the-art Ru-based electrocatalysts. g) Schematic diagram of the AEMWE device. h) Voltage–current curves of the AEMWE measured at room temperature (25 °C) using HNC-$RuCl_3$-300A or commercial Pt/C as the cathodic catalysts, along with RuO_2 as the anode catalysts. i) Variation of the cell voltage of the HNC-$RuCl_3$-300A or Pt/C based AEMWE at 500 mA cm^{-2} during 100 h's continuous operation.

($R_{ct} = 3.9\ \Omega$ at the overpotential of −100 mV, Figure 4d inset), in comparison to HNC-$RuBr_3$-300A (88.2 Ω), and HNC-RuI_3-300A (>105 Ω). Remarkably, HNC-$RuCl_3$-300A also showed excellent stability and durability. As shown in Figure 4e, almost no decay was observed for 10 h's continuous operation at the current density of 10 mA cm^{-2}, whereas η_{10} increased by −19 mV for commercial Pt/C; and HNC-$RuCl_3$-300A exhibited a decay of only 5 mV after 5000 potential cycles within the range of −50 to 0 mV (Figure 4e inset). In fact, XPS measurements of the HNC-$RuCl_3$-300A sample after the stability test showed virtually no change of the binding energy and elemental composition except for a slight decrease of the metal-Cl content to 0.29 at% (Figure S13, Table S1–S3, Supporting Information). This is further validated by in situ XAS measurements (Figure S14, Supporting Information), where the spectral features remained virtually unchanged with the electrode potential varied from 0 to −300 mV (Figure S15–S16, Table S5, Supporting Information). This remarkable durability is consistent with the low VBM of HNC-$RuCl_3$-300A (Figure 2i). Notably, HNC-$RuCl_3$-300A is highly comparable/to relevant catalysts reported recently in the literature (Figure 4f and Table S6, Supporting Information), such as Ru@NC ($\eta_{10} = -26$ mV),[51] mRu@PANI/CP (−27 mV),[52] and $RuSe_2$ (−29.5 mV).[53]

To explore the application of HNC-$RuCl_3$-300A in water splitting, the HNC-$RuCl_3$-300A sample was integrated into an AEMWE cell as the cathode catalyst (with commercial RuO_2 as the anodic catalyst, separated by an anion exchange membrane). The system was enclosed with bipolar stainless-steel plates for structural stability and efficient operation (Figure 4g). Figure 4h

displays the current–voltage curves for the HNC-$RuCl_3$-300A and commercial Pt/C based AEMWE cells at room temperature (25 °C). Notably, the HNC-$RuCl_3$-300A based AEMWE achieved a current density of 0.5 A cm^{-2} at a voltage of 1.88 V, which was significantly lower than that (2.24 V) required for the commercial Pt/C based counterpart. Remarkably, after 100 h's continuous operation, the HNC-$RuCl_3$-300A based AEMWE exhibited an almost invariant voltage of ≈1.94 V to produce 0.5 A cm^{-2}, whereas the Pt/C-based AEMWE experienced a notable voltage decay of ≈200 mV (Figure 4i). These results highlight the potential of HNC-$RuCl_3$-300A for practical AEMWE applications.

Notably, in comparison to HNC-$RuCl_3$ nanocomposites prepared at other induction currents (from 200 to 600 A) (Figure S5b and S17–S23, Table S1–S4, Supporting Information), HNC-$RuCl_3$-300A also exhibited a markedly enhanced HER performance (Figure S24–S25, Supporting Information), suggesting that 300A represented the optimal synthetic condition. HNC-$RuCl_3$-300A also showed a remarkable HER activity ($\eta_{10} = -81$ mV) in 0.5 M H_2SO_4, as compared to −160 mV for HNC-$RuBr_3$-300A and −333 mV for HNC-RuI_3-300A, but somewhat inferior to that of Pt/C (−34 mV) (Figure S26, Supporting Information).

Remarkably, the composite samples also exhibited apparent HOR activity. **Figure 5**a shows the HOR polarization curves in H_2-saturated 0.1 M KOH, where it can be clearly seen that the anodic current increased markedly in the order of HNC-RuI_3-300A < HNC-$RuBr_3$-300A < Pt/C < HNC-$RuCl_3$-300A at electrode potentials up to +0.1 V. In addition, HNC-$RuCl_3$-300A exhibited the lowest half-wave potential ($E_{1/2}$) of +18 mV, as compared to +23 mV for HNC-$RuBr_3$-300A, +25 mV for HNC-RuI_3-300A, and +35 mV for Pt/C. Moreover, HNC-$RuCl_3$-300A exhibited a high steady-state anodic current density of 2.02 mA cm^{-2}, which exceeded those of HNC-$RuBr_3$-300A (1.06 mA cm^{-2}) and HNC-RuI_3-300A (0.28 mA cm^{-2}), and was comparable to that of commercial Pt/C (2.10 mA cm^{-2}). In fact, HNC-$RuCl_3$-300A stood out again as the best HOR catalyst among the sample series (Figure S27, Supporting Information).

To investigate the reaction kinetics, the HOR polarization curves were collected with the rotation rates varied from 400 to 2500 rpm (Figure 5b and Figure S27–S28, Supporting Information), where the limiting current density increased with rotation rates. Figure 5c shows the corresponding Koutecky–Levich plot of HNC-$RuCl_3$-300A at +75 mV. Linear regression yielded a slope of 4.785 cm^2 mA^{-1} $s^{1/2}$ (Equation (1)), which was in excellent agreement with the theoretical value of 4.87 cm^2 mA^{-1} $s^{1/2}$ expected for the two-electron transfer of HOR.[54] Figure 5d depicts the kinetic current density (j_k) of the catalysts, obtained by fitting with the Butler–Volmer equation (Equation (2)), from which the exchange current density (j_0) was derived from linear fitting within the micro-polarization region (from −5 to +5 mV, Figure 5e).[55] Among the sample series, HNC-$RuCl_3$-300A exhibited the highest j_0 of 2.00 mA cm^{-2}, significantly surpassing HNC-$RuBr_3$-300A (0.81 mA cm^{-2}), HNC-RuI_3-300A (0.17 mA cm^{-2}), and Pt/C (0.99 mA cm^{-2}), confirming its outstanding HOR performance. In addition, HNC-$RuCl_3$-300A exhibited enhanced HOR stability with a 36.2% decay of the

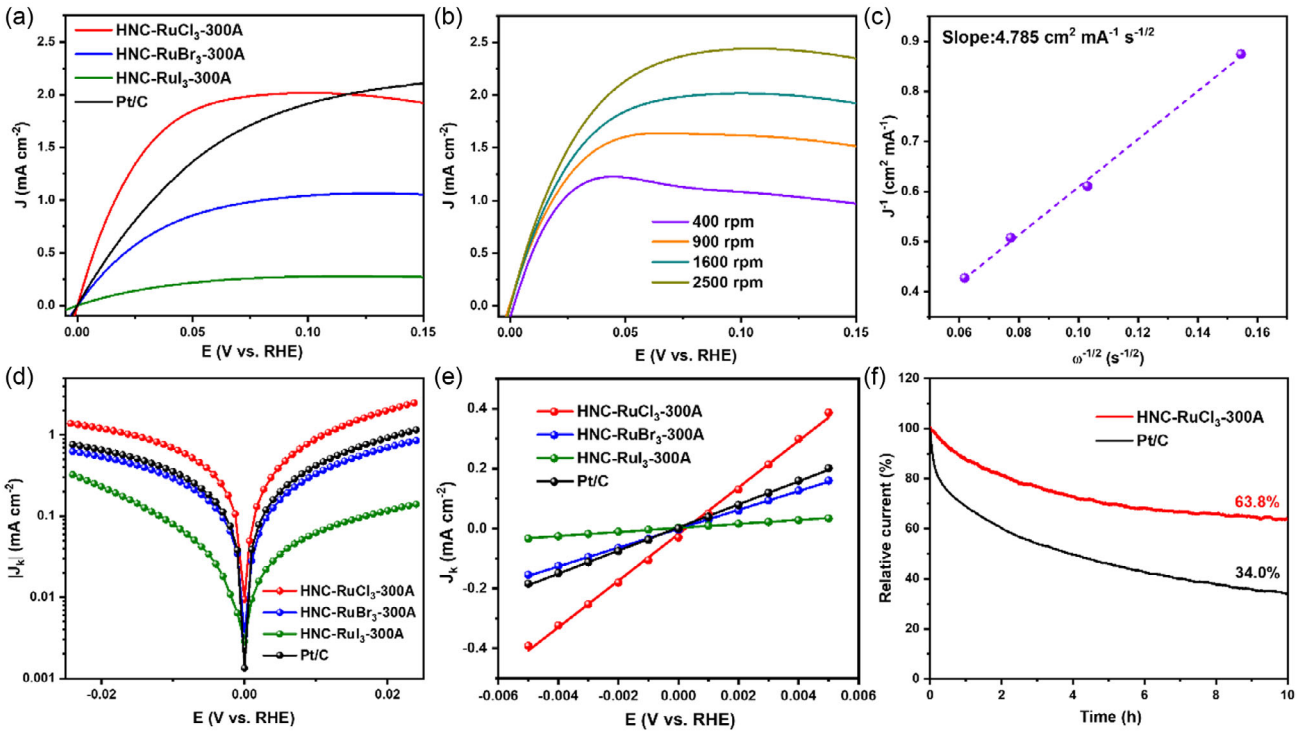

Figure 5. a) HOR polarization curves of HNC-$RuCl_3$-300A, HNC-$RuBr_3$-300A, HNC-RuI_3-300A, and commercial Pt/C in H_2-saturated 0.1 M KOH at a scan rate of 10 mV s^{-1} and a rotating rate of 1600 rpm. b) HOR polarization curves at various rotating speeds of HNC-$RuCl_3$-300A. c) Koutecky–Levich plot at +75 mV. d) Tafel plots with the Butler–Volmer fitting curves. e) Linear fitting curves in the micro-polarization region (from −5 to +5 mV). f) Relative current chronoamperometry of HNC-$RuCl_3$-300A and Pt/C in H_2-saturated 0.1 M KOH.

anodic current, as compared to 66.0% for Pt/C after 10 h's continuous operation (Figure 5f).

2.3. Computational Study

Results from the above experimental measurements suggest that nanoparticle size and halogen residues played a critical role in the determination of the electrocatalytic activity. DFT calculations were therefore performed to unravel the mechanistic insights. Due to the difference of the Ru nanoparticle size among the samples (Figure 1), a Ru_{48} cluster was used to model the HNC-$RuCl_3$-300A sample (while a larger cluster is preferred to model the actual Ru nanoparticles, this is a compromise due to limitation of computing resources), whereas a Ru(101) slab (Ru-101) for HNC-$RuBr_3$-300A and HNC-RuI_3-300A. Adsorption of H was then evaluated on varied sites of the structural models (Figure S29–S30, Supporting Information). Notably, for the Ru-101 slab, when an H atom is initially placed on top of a Ru atom, it moves quickly to the hollow site after relaxation, indicating that hollow site adsorption is the energetically preferred configuration, in contrast to Ru_{48} clusters, where on-top adsorption is possible.[30] **Figure 6**a and S31–S35 (Supporting Information display the H adsorption on the Ru_{48} cluster and Ru-101 slab without and with halide residues (symbols h and t refer to hollow and tetrahedral sites, respectively), and the corresponding Gibbs free energy of H adsorption (ΔG_{H^*}), a widely accepted descriptor of HER activity, was then evaluated. Generally, a $|\Delta G_{H^*}|$ close to 0 eV is deemed as an optimal condition for H adsorption and desorption, leading to maximal HER activity. One can see that pristine Ru-101 exhibits a rather high $|\Delta G_{H^*}|$ of $|-0.53|$ eV, suggesting somewhat too strong H adsorption which will render H_2 desorption difficult (Figure 6b), and a markedly reduced $|\Delta G_{H^*}|$ is observed with a decreasing size of the Ru clusters (Figure S29 and Table S7, Supporting Information). For instance, $|\Delta G_{H^*}|$ is only $|-0.073|$ eV for the edge site of the Ru_{48} cluster. This suggests that nanosized clusters are preferred for HER electrocatalysis. In addition, with the modification of a halogen atom, the $|\Delta G_{H^*}|$ becomes lower on both the cluster (Ru_{48}—Cl) and slab surfaces (i.e., Ru-101-hBr and Ru-101-hI). Specifically, the Ru_{48}-Cl edge site exhibits a $|\Delta G_{H^*}|$ of only $|-0.043|$ eV, whereas Ru-101-hBr and Ru-101-hI feature a similar $|\Delta G_{H^*}|$ of ca. $|-0.42|$ eV on the tetrahedral sites (Table S8, Supporting Information). These results suggest that the remarkable HER/HOR activity of HNC-$RuCl_3$-300A most likely arose from the combined contributions of reduced nanoparticle size and residual Cl modification, as compared to HNC-$RuBr_3$-300A and HNC-RuI_3-300A.

To further clarify the electronic structure of the atomic species, the total density of states (DOS) and projected DOS (PDOS) of the d electrons of Ru were calculated. As shown in Figure S36 (Supporting Information), the cluster and slab models all exhibit an almost identical pattern of the total DOS, suggesting a similar electronic feature around the Fermi level. Additionally, from the PDOS of the Ru active sites (Figure 6c), one can see that the Ru d band center (E_d) is situated at −1.37 eV for the Ru_{48} surface, and downshifts markedly to ca. −1.80 eV upon the addition of one Cl

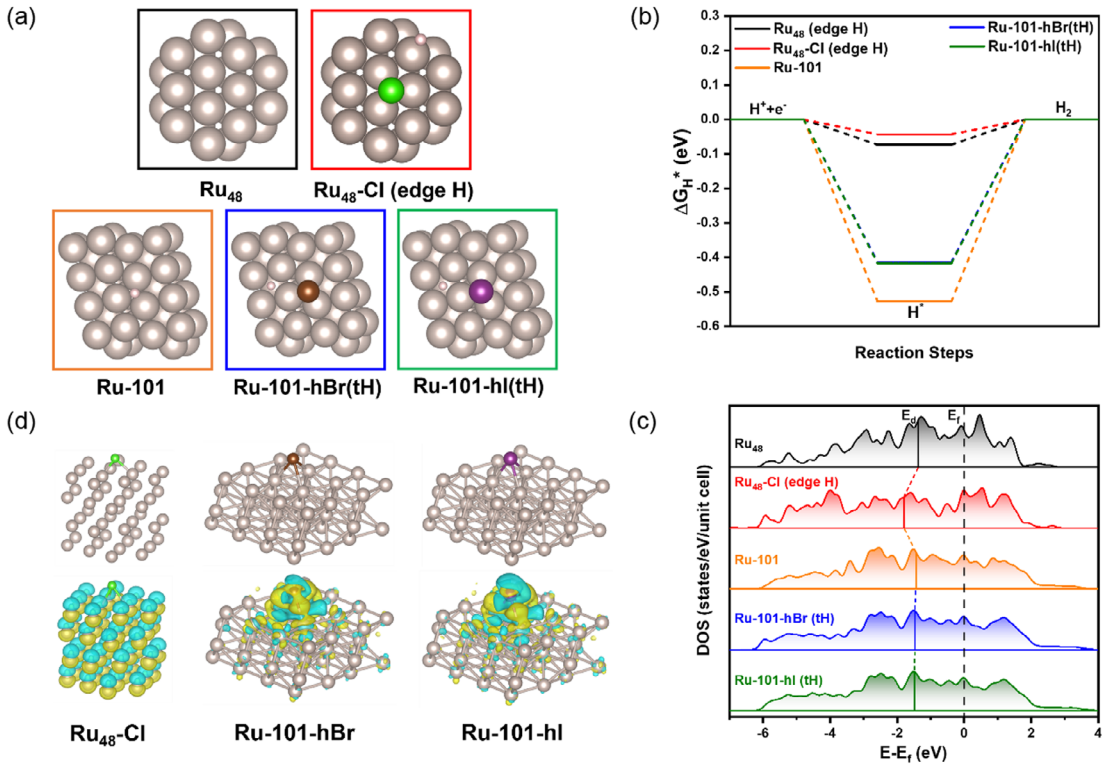

Figure 6. a) Computational relaxed models with diverse species: naked Ru_{48} cluster, Cl-modified Ru_{48} cluster (Ru_{48}-Cl), naked Ru-101 slab, and Ru-101 slab modified with a Br or I atom. Symbols h and t refer to hollow and tetrahedral sites, respectively. b) Gibbs free energy of H* adsorption (ΔG_{H^*}) on the corresponding models. c) PDOS of the d electrons of Ru active sites in the various models. d) Charge density distributions for the varied models. The cyan and yellow areas signify electron loss and electron gain, respectively. The isovalue of charge density is 0.001e $Bohr^{-3}$.

atom (Ru_{48}-Cl, edge H), indicating a weakened bonding interaction between the Ru surface and H by the Cl residue according to the d-band model.[24,25] By contrast, the impact of Br and I residues on the E_d of Ru(101) is minimal, which is estimated to be −1.41 eV for Ru(101), −1.47 eV for Ru-101-hBr (tH), and −1.47 eV for Ru-101-hI (tH). That is, Ru_{48}-Cl is anticipated to exhibit the weakest adsorption of H among the series (Figure 6b).

Bader charge analysis was then conducted to investigate the interactions between Ru and residual halogen species based on the differential charge density maps in Figure 6d. One can see that the halogen residues markedly induce charge transfer from the Ru cluster or Ru slab to halogen atoms, and the impacts vary with the halogen atoms. Specifically, one Cl atom withdraws 0.47 electrons from Ru_{48}, but only 0.33 and 0.13 electrons from the Ru slab by Br and I, respectively. This can be ascribed to the difference in electronegativity among the halogen atoms and is in good agreement with the Ru binding energy (valence state) observed in the above XPS measurements. Taken together, the charge transfer from Ru to halogen residues leads to a downshift of the Ru E_d and hence weakened H adsorption on the Ru active sites, where the impacts vary in the order of Cl > Br > I, consistent with the enhanced HER activity observed experimentally.

3. Conclusion

In this study, carbon-supported Ru nanoparticles were prepared by ultrafast synthesis with MIH at selected induction currents for 10 s. The produced HNC-RuX_3-300A composites consisted of Ru nanoparticles decorated with halogen residues, where the nanoparticle size increased and halogen content decreased from HNC-$RuCl_3$-300A to HNC-RuI_3-300A, due largely to the different thermal stability of the RuX_3 precursors. Among the series, HNC-$RuCl_3$-300A stood out as the best catalyst for both HER and HOR in alkaline media and even outperformed commercial Pt/C. Furthermore, HNC-$RuCl_x$-300A displayed a remarkable activity and stability in the AEMWE tests, as compared to the Pt/C based counterpart. Results from DFT studies confirmed that the surface halogen residues induced charge transfer from Ru, leading to a downshift of the Ru E_d and hence weakened H adsorption. Notably, the impacts were most pronounced with Cl and diminished drastically with Br and I residues. This is consistent with the experimental observation that HNC-$RuCl_3$-300A displayed the highest electrocatalytic activity among the series. Results from this study highlight the unique significance of nanoparticle size and heteroanion residues in the manipulation of the structure and activity of functional composites as high-performance catalysts for electrochemical energy technologies.

4. Experimental Section

Preparation of HNC-RuX_3-Y Composites

HNC was prepared by pyrolysis of hollow ZIF-8 derived from tannic acid etching of ZIF-8 (details in the Supporting Information).[31,56] 25 mg of the HNC powders was then dispersed into 5 mL of a RuX_3 solution (X = Cl, Br, and I) at the concentration of 1.25, 2.0 and 2.44 mg mL^{-1} for $RuCl_3{\cdot}xH_2O$, $RuBr_3{\cdot}xH_2O$ and RuI_3, respectively (corresponding to a final Ru loading of 10 wt%) under sonication for 30 min and then freeze-dried for 24 h. The obtained precursors were transferred onto an iron sheet (2.5 cm × 2.5 cm × 0.2 mm) and covered with graphite paper, which was then placed in a quartz tube and purged with nitrogen for 10 min. The quartz tube was then placed in the center of a four-turn induction coil with a diameter of 5 cm for MIH treatment at a controlled current (Y = 200–600 A) for 10 s (Figure S1, Supporting Information). The prepared powders were referred to as HNC-RuX_3-Y.

The corresponding controlled samples were prepared from the same freeze-dried precursors but in a tube furnace at 700 °C in a nitrogen atmosphere and denoted as HNC-RuX_3-TF700.

Characterizations

TEM images were collected with a Tecnai G2 instrument operated at 200 kV. HAADF-STEM images were obtained with a ThemIS scope operated at 60 kV. EDS measurements were conducted with a JEOL 2100-F scope operated at 200 kV. In situ XRD patterns were obtained with a Bruker D_8 Advance diffractometer using Cu K_α radiation (λ = 0.15418 nm). XPS was acquired with a Thermo Fisher K-Alpha system with the binding energy calibrated against that of C 1*s* electrons. Nitrogen adsorption/desorption isotherms were collected with a Micromeritics Tristar 3020 Porosimeter system at 77.3 K. Ex situ XAS measurements were carried out at 10 K at beamline 4–1 of the Stanford Synchrotron Radiation Lightsource using an Oxford liquid helium cryostat. In situ XAS measurements were performed at room temperature in a homemade cell equipped with a three-electrode setup filled with an appropriate electrolyte (Figure S13, Supporting Information).[32] X-rays passed through the samples from the Mylar windows under the controlled potentials. The collected XAS data were reduced, fitted, and interpreted using the RSXAP software.[57] The Fourier Transform and fitting ranges were 3.5–12.5 $Å^{-1}$ and 1.2–3.0 Å for the Ru K edge, respectively. The theoretical functions for Ru—O and Ru—Ru pairs were calculated by WebAtoms using FEFF7 software.[58]

Electrochemistry

Electrochemical measurements were performed with a CHI 710 E electrochemical workstation in a three-electrode configuration consisting of a Ag/AgCl (in acidic media) or Hg/HgO (in alkaline media) reference electrode, a graphite rod counter electrode, and a glassy carbon rotating disk working electrode. The Ag/AgCl and Hg/HgO reference electrodes were calibrated against a reversible hydrogen electrode (RHE), and all the potentials in the present study were referenced to the RHE. To prepare the working electrode, 2 mg of the nanocomposites prepared above were dispersed in a mixture of 250 μL of H_2O, 740 μL of isopropanol, and 10 μL of Nafion under sonication for 30 min, and 20 μL of the ink was drop-cast onto the pre-polished glassy carbon electrode (diameter 5 mm, area 0.196 cm^2) and dried naturally at room temperature before being coated with 5 μL of 20 wt% Nafion. The resulting catalyst loading was ≈0.204 mg cm^{-2}.

The HER polarization curves were acquired in 0.5 M H_2SO_4 or 1 M KOH at the scan rate of 10 mV s^{-1} with 90% iR compensation. Cyclic voltammetric (CV) measurements were performed in the non-Faradic potential range to estimate the double-layer capacitance (C_{dl}). Electrochemical impedance spectroscopy tests were conducted within the frequency range of 0.1–10^5 Hz at an alternating current (AC) amplitude of 5 mV at select overpotentials (−20, −50, and −100 mV). Chronopotentiometry tests were performed at the

constant current density of 10 mA cm^{-2} for 30 000 s. For CO stripping analysis,[59] the working electrode was immersed into a CO-saturated 1 M KOH solution at the potential of +0.05 V for 10 min, and then transferred into a N_2-saturated 1 M KOH solution where voltammetric measurements were conducted within the potential range of 0 to +1.0 V at a scan rate of 10 mV s^{-1}.

HOR tests were carried out in a H_2-saturated 0.1 M KOH aqueous solution at the potential scan rate of 10 mV s^{-1} and varied rotation rates (rpm) with a 95% iR correction. The kinetic current density (j_K) was determined using the Koutecky–Levich equation,

$$\frac{1}{j} = \frac{1}{j_K} + \frac{1}{j_D} \quad (1)$$

where j represents the measured current density, and j_D denotes the diffusion-limited current density. The exchange current density (j_0) was obtained by fitting j_k to the Butler–Volmer equation:

$$j_K = j_0 \left[\exp\left(\frac{\alpha F \eta}{RT}\right) - \exp\left(\frac{-(1-\alpha)F\eta}{RT}\right) \right] \quad (2)$$

where R is the gas constant (8.314 J mol^{-1} K^{-1}), F is the Faraday's constant (96 485 C mol^{-1}), α is the transfer coefficient, and T is the temperature (298.15 K).

AEMWE Tests

An AEMWE cell with an active area of 1.0 cm^2 was assembled, consisting of an HNC-$RuCl_3$-300A cathode and a commercial RuO_2 anode. The anion exchange membrane, Fumasep FAS-PET-75 (Fuel Cell Store), was pretreated by soaking in 0.5 M NaCl for 3 d followed by 1 M KOH for three additional days, before being thoroughly rinsed and stored in deionized water. The HNC-$RuCl_3$-300A and RuO_2 catalysts were dispersed in a solution containing 250 μL of H_2O, 740 μL of isopropanol, and 10 μL of Nafion. The resulting catalyst inks were sonicated for 30 min and then uniformly air-brushed onto a carbon paper gas diffusion layer, achieving a catalyst loading of 3 mg cm^{-2} for both the cathode and anode. The membrane electrode assembly (MEA) was then constructed by sandwiching the anode catalyst layer, anion exchange membrane, and cathode catalyst layer together. This MEA was further enclosed between two bipolar stainless-steel plates with embedded graphite plates, which featured 2 mm parallel channel flow fields. The electrolyte solution (1.0 M KOH) was recirculated through both cathode and anode at a flow rate of 10 mL min^{-1}. The stability was evaluated by monitoring the cell voltage changes at a current density of 0.5 A cm^{-2}.

Computational Study

DFT calculations were carried out using Quantum ESPRESSO, an open-source plane-wave code.[60] Ru cluster models and periodic slab surface models were constructed to simulate the experimental nanoparticle systems with varied sizes. Three Ru clusters of 36, 48, and 66 Ru atoms were built to investigate size effects of nanoparticles, with Ru_{48} selected to model the HNC-$RuCl_3$-300A system. A 4 × 4 surface unit cell with 48 atoms was used to build a Ru(101) slab supercell to study H adsorption on extended surfaces, where interactions between periodic images normal to the surface were removed by setting a vacuum of 15 Å. This slab model was used to simulate HNC-$RuBr_3$-300A and HNC-RuI_3-300A. Adsorption of H was evaluated on varied sites of these systems with and without the presence of a halide adatom, as a model for halide residues. We adopted the Perdew–Burke–Ernzerhof exchange-correlation functional with van der Waals interactions by using the DFT-D3 method. The Garrity-Bennett-Rabe-Vanderbilt (GBRV) ultra-soft pseudopotential with a cut-off of 50 and 500 Ry for kinetics and charge density was chosen.[61] The Brillouin zone was sampled by a 4 × 4 × 1 Monkhorst-Pack k-point mesh for the slab models, while only Γ-point was used for the cluster models. The total energy was calculated at the convergence level of 1 meV per atom. The smearing parameter was set at 0.01 Ry in the Marzari–Vanderbilt scheme for all calculations.[62] For geometric relaxation, the convergence criterion was 10^{-8} Ry for the electronic energy and 10^{-4} Ry $Bohr^{-1}$ for the total force. Density functional perturbation theory was employed to calculate the phonon frequency, which was then used as input to determine the Gibbs free energy.[63]

Acknowledgements

This work was supported by the National Science Foundation (grant nos. CHE-1900235 and CHE-2003685). TEM, XPS, and BET studies were conducted as part of a user project at the National Center for Electron Microscopy and Molecular Foundry, Lawrence Berkeley National Laboratory, which is supported by the Office of Science, Office of Basic Energy Sciences, of the U.S. Department of Energy under contract no. DE-AC02-05CH11231. XAS measurements were performed at the Stanford Synchrotron Radiation Lightsource (SSRL), which is also supported by the U.S. Department of Energy, Office of Science, Office of Basic Energy Sciences under contract no. DE-AC02-76SF00515. Computational work was carried out using the UCSC Lux Supercomputer, which is funded by the NSF MRI program (grant no. AST-1828315).

Conflict of Interest

The authors declare no conflict of interest.

Data Availability Statement

The data that support the findings of this study are available from the corresponding author upon reasonable request.

Keywords: anion exchange membrane water electrolyzers · halide residues · hydrogen evolution reactions · hydrogen oxidation reactions · ruthenium/carbon nanocomposites

[1] S. Singh, S. Jain, P. S. Venkateswaran, A. K. Tiwari, M. R. Nouni, J. K. Pandey, S. Goel, *Renewable Sustainable Energy Rev.* **2015**, *51*, 623.
[2] S. E. Hosseini, M. A. Wahid, *Renewable Sustainable Energy Rev.* **2016**, *57*, 850.
[3] M. A. Aminudin, S. K. Kamarudin, B. H. Lim, E. H. Majilan, M. S. Masdar, N. Shaari, *Int. J. Hydrogen Energy* **2023**, *48*, 4371.
[4] M. G. Surer, H. T. Arat, *Int. J. Hydrogen Energy* **2022**, *47*, 19865.
[5] N. Armaroli, V. Balzani, *ChemSusChem* **2011**, *4*, 21.
[6] A. Kovac, D. Marcius, L. Budin, *Int. J. Hydrogen Energy* **2019**, *44*, 9841.
[7] W. D. Gu, Z. Y. Yan, *Int. J. Hydrogen Energy* **2012**, *37*, 737.
[8] Q. Y. Jin, B. W. Ren, D. Q. Li, H. Cui, C. X. Wang, *Nano Energy* **2018**, *49*, 14.
[9] Q. Zhou, G. Q. Zhao, K. Rui, Y. P. Chen, X. Xu, S. X. Dou, W. P. Sun, *Nanoscale* **2019**, *11*, 717.
[10] Z. H. Pu, I. S. Amiinu, Z. K. Kou, W. Q. Li, S. C. Mu, *Angew. Chem., Int. Ed.* **2017**, *56*, 11559.
[11] J. Xu, J. B. Cui, C. Guo, Z. P. Zhao, R. Jiang, S. Y. Xu, Z. B. Zhuang, Y. Huang, L. Y. Wang, Y. D. Li, *Angew. Chem., Int. Ed.* **2016**, *55*, 6502.

[12] C. Cai, K. Liu, Y. M. Zhu, P. C. Li, Q. Y. Wang, B. Liu, S. Y. Chen, H. J. W. Li, L. Zhu, H. M. Li, J. W. Fu, Y. Chen, E. Pensa, J. H. Hu, Y. R. Lu, T. S. Chan, E. Cortés, M. Liu, *Angew. Chem., Int. Ed.* **2022**, *61*, 202113664.
[13] D. Zhang, Z. C. Wang, X. K. Wu, Y. Shi, N. Z. Nie, H. Zhao, H. F. Miao, X. L. Chen, S. X. Li, J. P. Lai, L. Wang, *Small* **2022**, *18*, 2104559.
[14] Y. Q. Li, X. Liu, J. L. Xu, S. R. Chen, *Small* **2024**, *20*, 2402846.
[15] Y. Q. Li, J. Y. Chen, Z. A. Wang, S. R. Chen, *ACS Appl. Nano Mater.* **2024**, *7*, 7555.
[16] J. K. Norskov, T. Bligaard, A. Logadottir, J. R. Kitchin, J. G. Chen, S. Pandelov, J. K. Norskov, *J. Electrochem. Soc.* **2005**, *152*, J23.
[17] Y. J. Yang, Y. H. Yu, J. Li, Q. R. Chen, Y. L. Du, P. Rao, R. S. Li, C. M. Jia, Z. Y. Kang, P. L. Deng, Y. J. Shen, X. L. Tian, *Nano-Micro Lett.* **2021**, *13*, 160.
[18] J. C. Zhang, G. B. Chen, Q. C. Liu, C. Fan, D. M. Sun, Y. W. Tang, H. J. Sun, X. L. Feng, *Angew. Chem., Int. Ed.* **2022**, *61*, e202209486.
[19] Q. L. Wu, M. Luo, J. H. Han, W. Peng, Y. Zhao, D. C. Chen, M. Peng, J. Liu, F. M. F. de Groot, Y. W. Tan, *ACS Energy Lett.* **2020**, *5*, 192.
[20] F. Yang, Y. Wang, Y. D. Cui, X. M. Yang, Y. M. Zhu, C. M. Weiss, M. H. Li, G. Y. Chen, Y. S. Yan, M. D. Gu, M. H. Shao, *J. Am. Chem. Soc.* **2023**, *145*, 27500.
[21] P. P. Su, W. Pei, X. W. Wang, Y. F. Ma, Q. K. Jiang, J. Liang, S. Zhou, J. J. Zhao, J. Liu, G. Q. Lu, *Angew. Chem., Int. Ed.* **2021**, *60*, 16044.
[22] C. F. Li, J. W. Zhao, L. J. Xie, Y. Wang, H. B. Tang, L. R. Zheng, G. R. Li, *J. Mater. Chem. A* **2021**, *9*, 12659.
[23] J. Wang, J. Liu, B. Y. Zhang, J. Gao, G. B. Liu, X. J. Cui, J. X. Liu, L. H. Jiang, *J. Mater. Chem. A* **2021**, *9*, 22934.
[24] J. K. Norskov, F. Abild-Pedersen, F. Studt, T. Bligaard, *Proc. Natl. Acad. Sci.* **2011**, *108*, 937.
[25] B. Hammer, J. K. Norskov, *Nature* **1995**, *376*, 238.
[26] Y. Zheng, Y. Jiao, Y. H. Zhu, L. H. Li, Y. Han, Y. Chen, M. Jaroniec, S. Z. Qiao, *J. Am. Chem. Soc.* **2016**, *138*, 16174.
[27] S. Y. He, Y. H. Tu, J. X. Zhang, L. H. Zhang, J. Ke, L. M. Wang, L. Du, Z. M. Cui, H. Y. Song, *Small* **2024**, *20*, 202308053.
[28] T. Y. Zhang, J. Jin, J. M. Chen, Y. Y. Fang, X. Han, J. Y. Chen, Y. P. Li, Y. Wang, J. F. Liu, L. Wang, *Nat. Commun.* **2022**, *13*, 6875.
[29] Z. X. Wu, Q. C. Li, G. R. Xu, W. Jin, W. P. Xiao, Z. J. Li, T. Y. Ma, S. H. Feng, L. Wang, *Adv. Mater.* **2024**, *36*, 202311018.
[30] Q. M. Liu, B. Z. Lu, F. Nichols, J. Ko, R. Mercado, F. Bridges, S. W. Chen, *SusMat* **2022**, *2*, 335.
[31] Q. M. Liu, Y. Peng, Q. X. Li, T. He, D. Morris, F. Nichols, R. Mercado, P. Zhang, S. W. Chen, *ACS Appl. Mater. Interfaces* **2020**, *12*, 17641.
[32] Q. M. Liu, S. McNair, F. Nichols, B. Z. Lu, B. Z. Yu, D. J. Pan, J. B. Ko, A. F. Bridges, S. W. Chen, *Adv. Sens. Energy Mater.* **2023**, *2*, 100046.
[33] B. Z. Lu, Q. M. Liu, C. Y. Wang, Z. Masood, D. J. Morris, F. Nichols, R. Mercado, P. Zhang, Q. F. Ge, H. L. L. Xin, S. W. Chen, *Research* **2022**, *2022*, 9756983.
[34] Y. X. Fan, X. D. Zhang, Y. J. Zhang, X. Xie, J. Ding, J. L. Cai, B. J. Li, H. L. Lv, L. Y. Liu, M. M. Zhu, X. C. Zheng, Q. Cai, Y. S. Liu, S. Y. Lu, *J. Colloid Interface Sci.* **2021**, *604*, 508.
[35] C. M. Li, S. T. Zhang, B. S. Zhang, D. S. Su, S. He, Y. F. Zhao, J. Liu, F. Wang, M. Wei, D. G. Evans, X. Duan, *J. Mater. Chem. A* **2013**, *1*, 2461.
[36] Y. R. Xue, L. Shi, X. R. Liu, J. J. Fang, X. D. Wang, B. P. Setzler, W. Zhu, Y. S. Yan, Z. B. Zhuang, *Nat. Commun.* **2020**, *11*, 5651.
[37] L. Falivene, A. Poater, C. S. J. Cazin, C. Slugovc, L. Cavallo, *Dalton Trans.* **2013**, *42*, 7312.
[38] K. S. W. Sing, D. H. Everett, R. A. W. Haul, L. Moscou, R. A. Pierotti, J. Rouquerol, T. Siemieniewska, *Pure Appl. Chem.* **1985**, *57*, 603.
[39] K. S. W. Sing, *Carbon* **1989**, *27*, 5.
[40] Q. Hu, K. R. Gao, X. D. Wang, H. J. Zheng, J. Y. Cao, L. R. Mi, Q. H. Huo, H. P. Yang, J. H. Liu, C. X. He, *Nat. Commun.* **2022**, *13*, 3958.
[41] X. P. Qin, L. L. Zhang, G. L. Xu, S. Q. Zhu, Q. Wang, M. Gu, X. Y. Zhang, C. J. Sun, P. B. Balbuena, K. Amine, M. H. Shao, *ACS Catal.* **2019**, *9*, 9614.
[42] P. Lokhande, P. L. Dhepe, *ACS Appl. Mater. Interfaces* **2023**, *15*, 47004.
[43] S. Sarkar, D. Mukherjee, R. Harini, G. Nagaraju, *J. Mater. Sci.* **2022**, *57*, 7680.
[44] F. Nichols, Q. M. Liu, J. Sandhu, Z. Azhar, R. Cazares, R. Mercado, F. Bridges, S. W. Chen, *J. Mater. Chem. A* **2022**, *10*, 5962.
[45] M. Wilson, R. Kore, A. W. Ritchie, R. C. Fraser, S. K. Beaumont, R. Srivastava, J. P. S. Badyal, *Colloid Surf., A* **2018**, *545*, 78.
[46] S. G. Ning, S. W. Zhang, J. N. Sun, C. P. Li, J. F. Zheng, Y. M. Khalifa, S. H. Zhou, J. Cao, Y. Y. Wu, *ACS Appl. Mater. Interfaces* **2020**, *12*, 43705.
[47] M. K. Rabchinskii, S. A. Ryzhkov, D. A. Kirilenko, N. V. Ulin, M. V. Baidakova, V. V. Shnitov, S. I. Pavlov, R. G. Chumakov, D. Y. Stolyarova, N. A. Besedina, A. V. Shvidchenko, D. V. Potorochin, F. Roth, D. A. Smirnov, M. V. Gudkov, M. Brzhezinskaya, O. I. Lebedev, V. P. Melnikov, P. N. Brunkov, *Sci. Rep.* **2020**, *10*, 6902.
[48] Y. Li, Z.-Z. Shen, G.-X. Liu, R. Wen, *Adv. Sens. Energy Mater.* **2022**, *1*, 100036.
[49] R. Liu, W. C. Tonjes, V. A. Greanya, C. G. Olson, R. F. Frindt, *Phys. Rev. B* **2000**, *61*, 5212.
[50] B. Z. Yu, Q. M. Liu, F. Nichols, K. Mayford, D. J. Pan, H. L. Kuo, J. Q. Lu, F. Bridges, S. W. Chen, *J. Phys. Chem. C* **2023**, *127*, 3996.
[51] Z. L. Wang, K. J. Sun, J. Henzie, X. F. Hao, C. L. Li, T. Takei, Y. M. Kang, Y. Yamauchi, *Angew. Chem., Int. Ed.* **2018**, *57*, 5848.
[52] Z. Y. Duan, M. Zhang, L. Cui, H. J. Yu, K. Deng, Y. Xu, Z. Q. Wang, L. Wang, H. J. Wang, *J. Mater. Chem. A* **2022**, *10*, 14435.
[53] Z. Zhang, C. Jiang, P. Li, K. G. Yao, Z. L. Zhao, J. T. Fan, H. Li, H. J. Wang, *Small* **2021**, *17*, 2007333.
[54] L. Yan, D. C. Wang, M. J. Li, R. H. Lu, M. G. Lu, P. P. Li, K. Y. Wang, S. Jin, Z. Y. Wang, S. B. Tian, *Angew. Chem., Int. Ed.* **2024**, *63*, 202410832.
[55] J. T. Zhang, M. F. Cao, X. T. Li, Y. Xu, W. Zhao, L. G. Chen, Y. C. Chang, C. W. Pao, Z. W. Hu, X. Q. Huang, *Small* **2023**, *19*, 202207038.
[56] Y. J. Chen, S. F. Ji, Y. G. Wang, J. C. Dong, W. X. Chen, Z. Li, R. A. Shen, L. R. Zheng, Z. B. Zhuang, D. S. Wang, Y. D. Li, *Angew. Chem., Int. Ed.* **2017**, *56*, 6937.
[57] C. H. Booth, F. Bridges, *Int. Tables Crystallogr.* **2024**, *1*, 822.
[58] B. Ravel, M. Newville, *J. Synchr. Radiat.* **2005**, *12*, 537.
[59] B. X. Zhang, B. H. Zhang, G. Q. Zhao, J. M. Wang, D. Q. Liu, Y. P. Chen, L. X. Xia, M. X. Gao, Y. F. Liu, W. P. Sun, H. G. Pan, *Nat. Commun.* **2022**, *13*, 5894.
[60] P. Giannozzi, S. Baroni, N. Bonini, M. R. Car, C. Cavazzoni, D. Ceresoli, G. L. Chiarotti, M. Cococcioni, I. Dabo, A. Dal Corso, S. de Gironcoli, S. Fabris, G. Fratesi, R. Gebauer, U. Gerstmann, C. Gougoussis, A. Kokalj, M. Lazzeri, L. Martin-Samos, N. Marzari, F. Mauri, R. Mazzarello, S. Paolini, A. Pasquarello, L. Paulatto, C. Sbraccia, S. G. Sclauzero, A. P. Seitsonen, et al., *J. Phys.: Condens. Matter* **2009**, *21*, 395502.
[61] K. F. Garrity, J. W. Bennett, K. M. Rabe, D. Vanderbilt, *Comput. Mater. Sci.* **2014**, *81*, 446.
[62] N. Marzari, D. Vanderbilt, A. De Vita, M. C. Payne, *Phys. Rev. Lett.* **1999**, *82*, 3296.
[63] S. Baroni, S. de Gironcoli, A. Dal Corso, P. Giannozzi, *Rev. Mod. Phys.* **2001**, *73*, 515.

Manuscript received: April 15, 2025
Revised manuscript received: May 19, 2025
Version of record online: June 17, 2025